PHYSICAL REVIEW E **110**, 034208 (2024)

# Topological phases in population dynamics with rock-paper-scissors interactions

Jinfeng Liang, Qionglin Dai,[*] Hancheng Li, Haihong Li, and Junzhong Yang[†]
*School of Science, Beijing University of Posts and Telecommunications, Beijing 100876, People's Republic of China*

(Received 3 March 2024; accepted 19 August 2024; published 12 September 2024)

Topological phases have arisen great interests of physicists. Though most works focus on quantum systems, topological phases can also be found in nonquantum systems. In this work, we study an antisymmetric Lotka-Volterra dynamics defined on a chain of two-site cells with open boundary conditions. We find two edge-localization states, left edge-localization state, and right edge-localization state. In an edge-localization state, there exists a boundary region in which mass distribution displays an exponential decay with the distance away from the boundary. The two edge-localization states are connected by a sharp transition. To comprehend the edge-localization states, we transform the population dynamics into a non-Hermitian quantum system. Based on the generalized topological band theory of the non-Hermitian system with periodic boundary conditions, we use winding number to distinguish the left and the right edge-localization states, and the transition between these two states is identified to be a topological one.

DOI: 10.1103/PhysRevE.110.034208

## I. INTRODUCTION

Recently, topological edge states in systems with open boundary conditions (OBC) have drawn great attention [1–5]. The investigations of topological effects in materials can be dated back to the quantum Hall effect [6,7] and topological band theory serves as a foundation to analyze these effects [8–10]. In systems possessing Hermitian symmetry, the topological band theory establishes the bulk-boundary correspondence to identify the topological edge states [11–14]. In bulk-boundary correspondence, topological invariants acquired in periodic boundary conditions (PBC) directly identifies the number of topologically edge states in OBC, and topological edge states with different topological invariants are different ones [15–20]. Only topological phases with the same topological invariant can be transformed without inducing a phase transition. Topological edge states are topologically protected against perturbations and weak disorder, which is behind its potential applications in photonic [21,22] and phononic systems [23].

It is well known that the nonreciprocal interaction or interaction with environment may lead a system to be non-Hermitian. In recent years, non-Hermitian systems have attracted a lot of attention. Many phenomena and features, which are completely different from Hermitian systems, have been discovered. Phenomena associated with exceptional points have been studied in pumped atoms [24]. Non-Hermitian skin effects (NHSE), which account for edge localization of states [25], are typical in systems with nonreciprocal interaction. Edge burst [26] occurs for quantum walkers on specific structures with OBC when the loss on sites is introduced. Furthermore, non-Hermitian many-body systems can also show NHSE and other noteworthy features [27]. However, traditional topological band theory fails for non-Hermitian systems due to the existence of the complex eigenvalues of non-Hermitian Hamiltonians. To generalize the topological band theory to the field of topological phenomena in non-Hermitian systems, Wang *et al.* [15] proposed the concept of generalized Brillouin zone, based on which topological invariants can be constructed, and rebuilt the generalized body-boundary correspondence. Using the generalized topological band theory, topological properties in non-Hermitian systems can be well described.

Non-Hermitian characteristics might be prevalent in ecological, economic, and social systems which are actually described as open systems. Then the question arises naturally of whether topological states such as edge states can be realized in these systems under proper conditions. Tang and colleagues [28] showed how stochastic systems with nonequilibrium cycles at the microscopic scale support chiral edge currents along the boundaries of the systems configuration space and ascribed the emergence of edge currents to a topological transition. Yoshida and colleagues [29] investigated a kagome network of rock-paper-scissors (RPS) and found a chiral edge mode of the population density which is protected by the nontrivial topology in the bulk. Knebel and colleagues [30] studied a one-dimensional chain of RPS cycles and found robust polarization states. Using the sign of the Pfaffian as a topological invariant, they identified the polarization states as topological ones. However, in these works, the correspondence between dynamical evolution rules and the non-Hermitian Hamiltonian is not clearly established, which makes the descriptions based on topological phases in quantum systems a little vague. Moreover, a proper topological invariant in these works is short, for example, the sign of Pfaffian cannot depict the number of different topological states as required by topological invariants. To solve these problems, we focus on a one-dimensional chain of RPS

---

[*] Contact author: qldai@bupt.edu.cn
[†] Contact author: jzyang@bupt.edu.cn

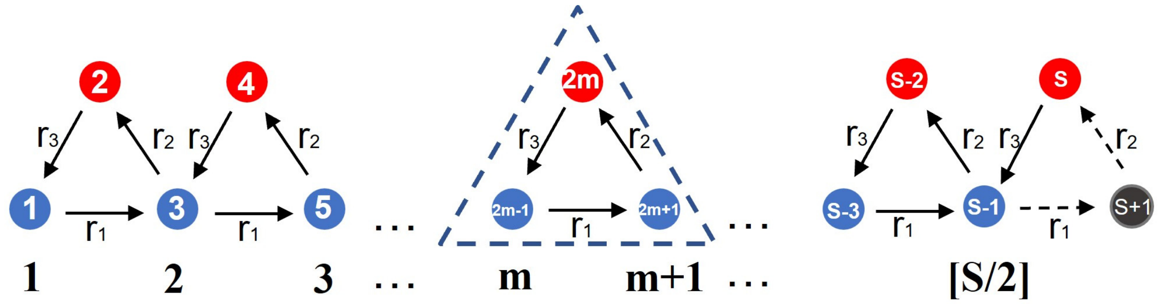

FIG. 1. Schematic diagram of the chain of two-site cells with cell $m$ consisting of sites $2m-1$ and $2m$ ($m = 1, 2, ..., n$ with $n = [S/2]$). The number in the circle is the node index, and the bottom number the cell index. Each triangle suggests a rock-paper-scissors interaction with $r_1$, $r_2$ the intercell interaction strengths and $r_3$ the intracell interaction strength. The site $S+1$ is the same one as site 1 in the case of periodic boundary condition.

cycles. After illustrating the edge mass localization in details by numerically simulating the mass evolution equations, we draw an effective non-Hermitian Hamiltonian based on on-site creation and annihilation operators, which gives rise to an evolution equation of number operator exactly as the mass evolution equation. Then, using generalized topological band theory, we present a proper topological invariant by using biorthogonal basis of the non-Hermitian Hamiltonian which identifies the edge mass localization states to be topological ones.

The rest of the paper is organized as follows. In Sec. II, we present the model. In Sec. III, we first present numerical results on the chain of RPS cycles. Then we establish the correspondence between the population dynamics and non-Hermitian quantum system. After that, we introduce a topological invariant, winding number, to identify different topological states. Furthermore, we study the topological phases by modifying the chain structures. Finally, a summary is presented in Sec. IV.

## II. MODEL

We consider an antisymmetric Lotka-Volterra equation (ALVE) defined on a network with $S$ sites. As is pictorially shown in Fig. 1, the network is characterized by a one-dimensional chain of $n = [S/2]$ two-site cells with $[\cdot]$ denoting floor. We consider two types of boundary conditions, PBC and OBC. For PBC, $S$ is an even number and site $S+1$ is exactly site 1, while $S$ is an odd number for OBC.

The mass at each site $i$ is denoted as $x_i$ and is evolved according to the coupled ordinary differential equations

$$\frac{d}{dt}x_i = x_i \sum_{j=1}^{S} a_{ij}x_j. \tag{1}$$

Here the parameter $a_{ij}$ represents the interaction strength between sites $i$ and $j$ and we require $a_{ij} = -a_{ji}$ which leads the model to be a conservative one. Following the RPS game rule, we let $a_{ij} = r_1$ if $i = 2m+1$ and $j = 2m-1$, $a_{ij} = r_2$ if $i = 2m$ and $j = 2m+1$, $a_{ij} = r_3$ if $i = 2m$ and $j = 2m-1$, and $a_{ij} = 0$ otherwise, where $m = 1, 2, ..., n$. Actually, the parameters $r_1$, $r_2$, and $r_3$ account for the intercell or intracell interaction strengths. Regarding this, there are two equivalent descriptions. On one hand, two-site cell $m$ consists of sites $2m-1$ and $2m$ ($m = 1, 2, ...n$). In this description, $r_3$ is the intracell interaction, while $r_{1,2}$ the intercell ones. On the other hand, two-site cell $m$ consists of sites $2m$ and $2m+1$ where $r_2$ is the intracell interaction, while $r_{1,3}$ the intercell ones. In these two descriptions, $r_1$ is always the intercell interaction. In contrast, $r_2$ and $r_3$ alternate their roles in the intracell and intercell interactions, which suggests that $r_2$ and $r_3$ would play similar effects on the model behaviors.

## III. RESULTS

### A. Numerical simulations on topological phases of the ALVE model

We consider the case of OBC. If we require $r_1$, $r_2$, and $r_3$ to be positive, as schematically shown in Fig. 1, $r_1$ induces mass flow from left to right ($r_1$ flow), which is characterized by the mass distribution on the subchain of sites $2m-1$ with $m$ the cell index, while $r_2$ and $r_3$ induce a mass flow ($r_3$ flow) in an opposite direction characterized by the mass distribution on the subchain of sites $2m$. The competition between these two mass flows determines the final mass distribution along the chain. To find the mass distribution, we numerically simulate the model (1) using fourth order Runge-Kutta algorithm with time step 0.01. Considering that a conservative system always gives rise to time-dependent solutions, we monitor the time-averaged mass $\langle x_i \rangle$ on each site which is defined as $\langle x_i \rangle = \frac{1}{T}\int_0^T x_i dt$ over a sufficient long time interval. To be noted, initial conditions do not influence the final distribution of $\langle x_i \rangle$.

As mentioned above, the $r_1$ flow is opposite to the $r_3$ flow, which suggests that the effects of interaction $r_1$ on the model behaviors could be quite different from interactions $r_2$ and $r_3$. For the sake of it, we first fix $r_1$ to be constant, i.e., $r_1 = 0.8$, and study the effects of $r_2$ and $r_3$ on the model behaviors. Figure 2(a) shows the mass distributions for different chain sizes at $r_2 = 1.2$ and $r_3 = 1$. As shown, the $r_3$ flow outperforms the $r_1$ flow, which results in mass localization around the left edge. In this mass localization state, there exist three distinct regions in the mass distribution for large chain size (i.e., $S = 101$), the boundary region, transition region, and the bulk region. In the boundary region, the mass decreases with the distance of cells away from the left edge in an exponential way for both the $r_1$ flow and $r_3$ flow subchains. The exponential mass distribution can be numerically

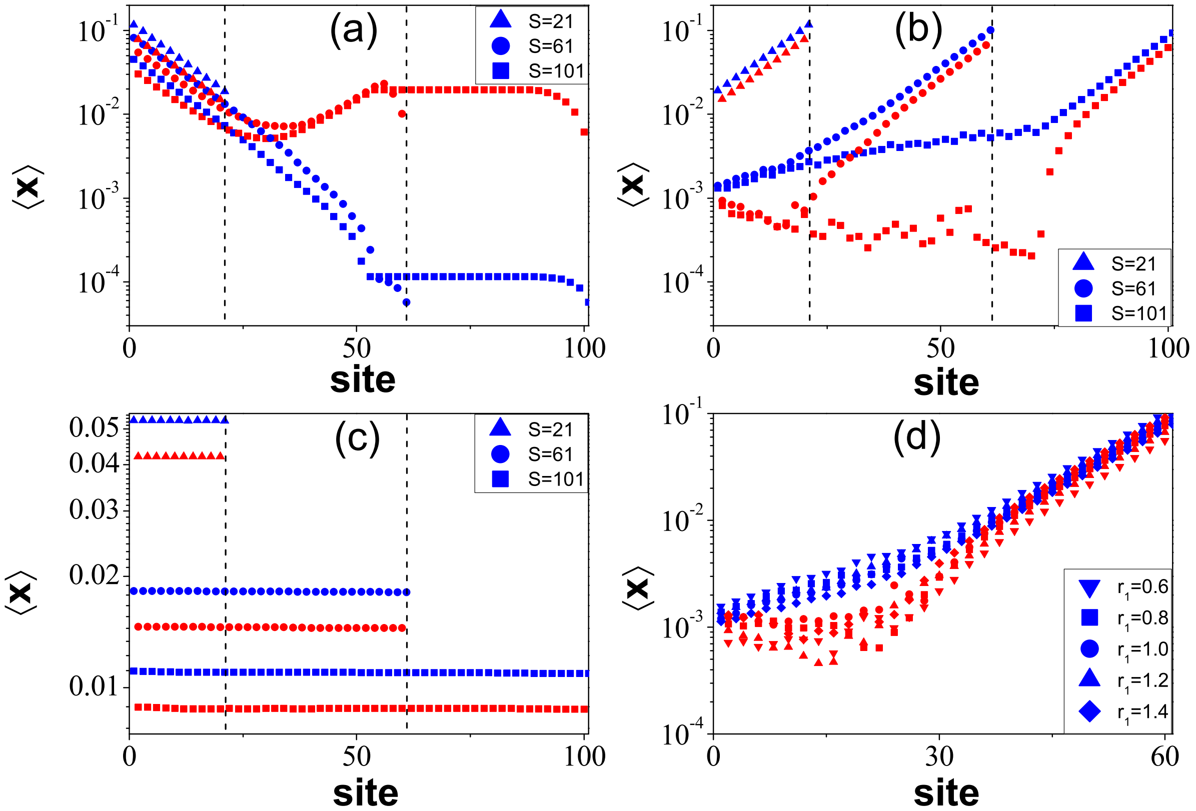

FIG. 2. Mass distribution of ALVE model under different system sizes and different parameters with the mass on the $r_1$-flow subchain in blue and on the $r_3$-flow subchain in red. The total mass is $\sum_{i=1}^{S} x_i = 1$ in simulations. (a) The left edge localization state for several system sizes at $r_1 = 0.8$, $r_2 = 1.2$, and $r_3 = 1$; (b) The right edge localization state for several system sizes with $r_1 = 0.8$, $r_2 = 1$, and $r_3 = 1.2$; (c) The uniform state with $r_1 = 0.8$, $r_2 = 1$, and $r_3 = 1$; (d) The right edge localization state at the system size $S = 61$, $r_2 = 1$, and $r_3 = 1.2$ for different $r_1$. Dash lines in panels (a)–(c) indicate site 21 (left dash lines) and site 61 (right dash lines).

described by $\langle x_i \rangle \sim ln(r_2/r_3)$ as an empirical formula [30]. In the transition region, the mass distributions along the $r_1$-flow and the $r_3$-flow subchains become separated from each other. The more the cell is away from the left edge, the more the two mass distributions of the site in this cell get separated. Particularly, the mass distribution over the $r_1$-flow subchains maintains the exponential variation as that in the boundary region. In the bulk region, the mass distribution becomes unchanged unless the cells are sufficiently close to the right edge. In addition, the mass localization state around the left edge is quite robust against the system size. For small size system, only boundary region exists. With the increase of the system size, the transition region and the bulk region appear successively. Especially, for sufficiently large system size, the distance between the delimitation of the boundary and the transition regions (or of the transition and the bulk regions) and the left edge is roughly unchanged with the variation of the system size.

However, the edge localization state does not always occur at the left edge. As shown in Fig. 2(b), as we switch the parameter for $r_2 = 1$ and $r_3 = 1.2$, the $r_1$ flow outperforms the $r_3$ flow and the edge localization state occurs at the right edge. Different from the left edge localization state, the mass distribution only displays two regions in the right edge localization state, the boundary, and the bulk regions in which the mass distribution of the $r_1$ subchain displays an exponential variation, which means $r_2$ and $r_3$ play different roles in the dynamic because they stand different beside the cell. Similar to the left edge localization state, the exponential mass distribution in the boundary region is maintained in the right edge localization state and, more importantly, the system size does not change the delimitation between the boundary and the bulk regions. Interestingly, the transition between the right and the left edge localization states occurs right at $r_2 = r_3$. Figure 2(c) shows one example at $r_2 = r_3 = 1$ where the edge localization states disappear and the mass uniformly distributes both on the $r_1$- and $r_3$ subchains. The uniform mass distributions suggest the $r_1$ and $r_3$ flows are balanced.

Furthermore, we consider the impact of $r_1$ on the edge localization states. In the limited situations with $r_1$ close to zero or sufficiently large $r_1$, the edge localization states disappear due to the absence of the competition between $r_1$- and $r_3$-mass flows. Therefore we focus on the intermediate $r_1$. In Fig. 2(d), we scrutinize the right edge localization states for several $r_1$ at $N = 61$. It can be seen that, though the characteristics of the edge localization states are preserved, varying $r_1$ alters the mass differentiation between the $r_1$- and the $r_3$ subchains. In other words, the intercell interaction strength $r_1$ impacts on the edge localization state by changing the mass distribution within the cells.

### B. Theoretical analysis on topological phases of the ALVE model

The edge localization states have been identified to be topological phases in model (1) by Knebel *et al.* [30]. The authors treated the interaction matrix $a_{ij}$ to be an effective Hamiltonian, and introduced a topological invariant, Pfaffian, to identify the transition between the left and the right edge localization states. Unfortunately, Pfaffian cannot provide the information on the number of distinct topological phases. Here, to explore the topological phases in model (1), we resort to the winding number, one topological invariant, by using of the non-Bloch band theory and biorthogonal bases proposed by Yao *et al.* [15,16] recently.

The properties of edge localization states in OBC can be inferred from the topological invariant in PBC (the body-edge correspondence). Using the interaction matrix ($a_{ij}$) in model (1) with $n$ cells, the effective Hamiltonian in PBC can be constructed as

$$\begin{aligned}\hat{H} = \sum_{i}^{n}(&r_3 a_i^\dagger b_i - r_3 b_i^\dagger a_i + r_1 a_{i-1}^\dagger a_i - r_1 a_{i+1}^\dagger a_i \\ &+ r_2 a_{i+1}^\dagger b_i - r_2 b_{i-1}^\dagger a_i)\end{aligned} \tag{2}$$

with $a_{n+1} = a_1$. Here, the subscript $i$ refers to the $i$th cell. $a_i$ and $a_i^\dagger$ denote the creation and annihilation operators at site $2i-1$ while $b_i$ and $b_i^\dagger$ the creation and annihilation operators at site $2i$. In terms of population dynamics, the number operator $a_i^\dagger a_i$ (or $b_i^\dagger b_i$) means the number of individuals at site $2i-1$ (or $2i$). In the Hamiltonian (2), the first term $r_3 a_i^\dagger b_i$ refers to the event that the individual at site $2i$ is predated by the one at $2i-1$ with a strength $r_3$, while the second term $-r_3 b_i^\dagger a_i$ refers to the inverse of the event that the individual at site $2i-1$ is predated by the one at $2i$ with a strength $r_3$. Therefore, the first two terms in the Hamiltonian represent the same predation interaction between individuals in a same cell. The last four terms on the right-hand side account for the interaction between adjacent cells. The effective Hamiltonian (2) provides a way to analyze the edge localization in the population dynamics (1) in the context of quantum mechanics.

Since Hamiltonian (2) possesses the transitional invariance, we may introduce annihilation operators $\widetilde{a}_k$ and $\widetilde{b}_k$ such that $a_i = \frac{1}{\sqrt{n}}\sum_k \widetilde{a}_k e^{-\mathrm{i}ki}$ and $b_i = \frac{1}{\sqrt{n}}\sum_k \widetilde{b}_k e^{-\mathrm{i}ki}$ with i the imaginary unit and $k = i2\pi/n$ $(i = 1, \ldots, n)$. Then the Hamiltonian (2) is reformulated as

$$\begin{aligned}H &= \sum_k (r_3 \widetilde{a}_k^\dagger \widetilde{b}_k - r_3 \widetilde{b}_k^\dagger \widetilde{a}_k + r_1 \widetilde{a}_k^\dagger \widetilde{a}_k e^{-ik} - r_1 \widetilde{a}_k^\dagger \widetilde{a}_k e^{ik} \\ &\quad + r_2 \widetilde{a}_k^\dagger \widetilde{b}_k e^{ik} - r_2 \widetilde{b}_k^\dagger \widetilde{a}_k e^{-ik}) \\ &= \sum_k (\widetilde{a}_k^\dagger, \widetilde{b}_k^\dagger)\widetilde{H}(k)(\widetilde{a}_k, \widetilde{b}_k)^T,\end{aligned} \tag{3}$$

with

$$\widetilde{H}(k) = \begin{pmatrix} r_1(e^{-\mathrm{i}k} - e^{\mathrm{i}k}) & r_3 - r_2 e^{-\mathrm{i}k} \\ -r_3 + r_2 e^{\mathrm{i}k} & 0 \end{pmatrix}, \tag{4}$$

the Bloch Hamiltonian. Here, $\widetilde{H}(k)$ is clearly not a Hermitian one since $\widetilde{H}(k)^\dagger = -\widetilde{H}(k)$. For each $k$, $\widetilde{H}(k)$ allows for two eigenvalues:

$$\begin{aligned}E^{\pm}(k) &= -ir_1 \sin k \\ &\quad \pm \sqrt{-r_1^2 \sin^2 k - r_2^2 \sin^2 k - (r_3 - r_2 \cos k)^2},\end{aligned} \tag{5}$$

with ± distinguishing the two energy bands.

The non-Hermitian Bloch Hamiltonian requires that the left and the right eigenvalue of its eigenvalue $E$ should be obtained differently as follows:

$$\begin{aligned}\widetilde{H}(k)|u_R(k)\rangle &= E(k)|u_R(k)\rangle, \\ \widetilde{H}^\dagger(k)|u_L(k)\rangle &= E^*(k)|u_L(k)\rangle,\end{aligned} \tag{6}$$

with $E^*$ being the complex conjugate of $E$. Therefore, the right and the left eigenvectors can be given as

$$\begin{aligned}|u_R^{\pm}(k)\rangle &= \begin{pmatrix} E^{\pm}(k) \\ -r_3 + r_2 \cos k + ir_2 \sin k \end{pmatrix}, \\ |u_L^{\pm}(k)\rangle &= \begin{pmatrix} E^{*,\pm}(k) \\ r_3 - r_2 \cos k - ir_2 \sin k \end{pmatrix}.\end{aligned} \tag{7}$$

Now using the left and the right eigenvectors $|u_R^{\pm}\rangle$ and $|u_L^{\pm}\rangle$, of the two energy bands $E^{\pm}$, we may present the formula for calculating the winding number. Winding number is a global measure of the topological nature of the band structure, which can be calculated by taking the line integral of a certain vector around a closed path. In one-dimensional case, line integral around the closed path reduces to the integral for $k$ ranging from 0 to $2\pi$ for all energy bands. For our model, we choose the certain vector to be the non-Abelian Berry connection $A^{\alpha\beta}$. By using the biorthogonal basis, $|u_R^{\pm}\rangle$ and $|u_L^{\pm}\rangle$, we generalize the definition of Berry connection in Ref. [13] such that

$$\mathcal{A}^{\alpha\beta}(k) = \langle u_L^{\alpha}(k)|\nabla_k u_R^{\beta}(k)\rangle, \tag{8}$$

in which $\alpha$ and $\beta$ take either + or −, denoting the energy bands, and $\nabla_k$ denotes the differentiation over $k$. Then the winding number can be calculated as follows:

$$W = -\frac{i}{2\pi}\int_0^{2\pi}\left(\frac{1}{\mathcal{A}^{++}}\frac{d\mathcal{A}^{++}}{dk} + \frac{1}{\mathcal{A}^{--}}\frac{d\mathcal{A}^{--}}{dk}\right)dk. \tag{9}$$

The winding number in Eq. (9) represents the quantize flux of the Berry field through a closed path of $k$ ranging from 0 to $2\pi$, which is analogous to the magnetic flux through a loop in a magnetic field.

Performing numerical integration, we examine the dependence of the winding number on the interaction strengths. We find that the topological phases only depend on the ratio $r_2/r_3$ with phase transition at $r_2/r_3 = 1$ and are independent of $r_1$. To exemplify it, we first consider $W$ against $r_2$ at $r_1 = 0.8$ and $r_3 = 1.2$. As shown in Fig. 3(a), $W$ can only take one integer out of $\{0, -2\}$, $W = 0$ for $r_2 < r_3$, and $W = -2$ for $r_2 > r_3$. At $r_2 = r_3$, $W$ jumps from 0 to −2. According to the bulk-boundary correspondence in the quantum topological phases theory [15], winding number acquired in PBC may dictate the properties of topological states in OBC. For example, integer winding number suggests a topological state while the maximum $|W|$ determines the number of possible topological states. Therefore, $W = -2$ in Fig. 3(a) indicates that there are two different topological states in model (1), which is exactly the left and the right edge localization states in Fig. 2. The jump of $W = 0$ to $W = -2$ at $r_2 = r_3$ in Fig. 3(a) suggests a sharp topological phase transition from the right edge localization state to the left one in Fig. 2. Winding number against $r_3$ in Fig. 3(b) further confirms the above results. In contrast, in Fig. 3(c) at $r_2 = r_3 = 1.2$ (the topological phase transition), $W$ varies continuously with $r_1$, which means a nontopological

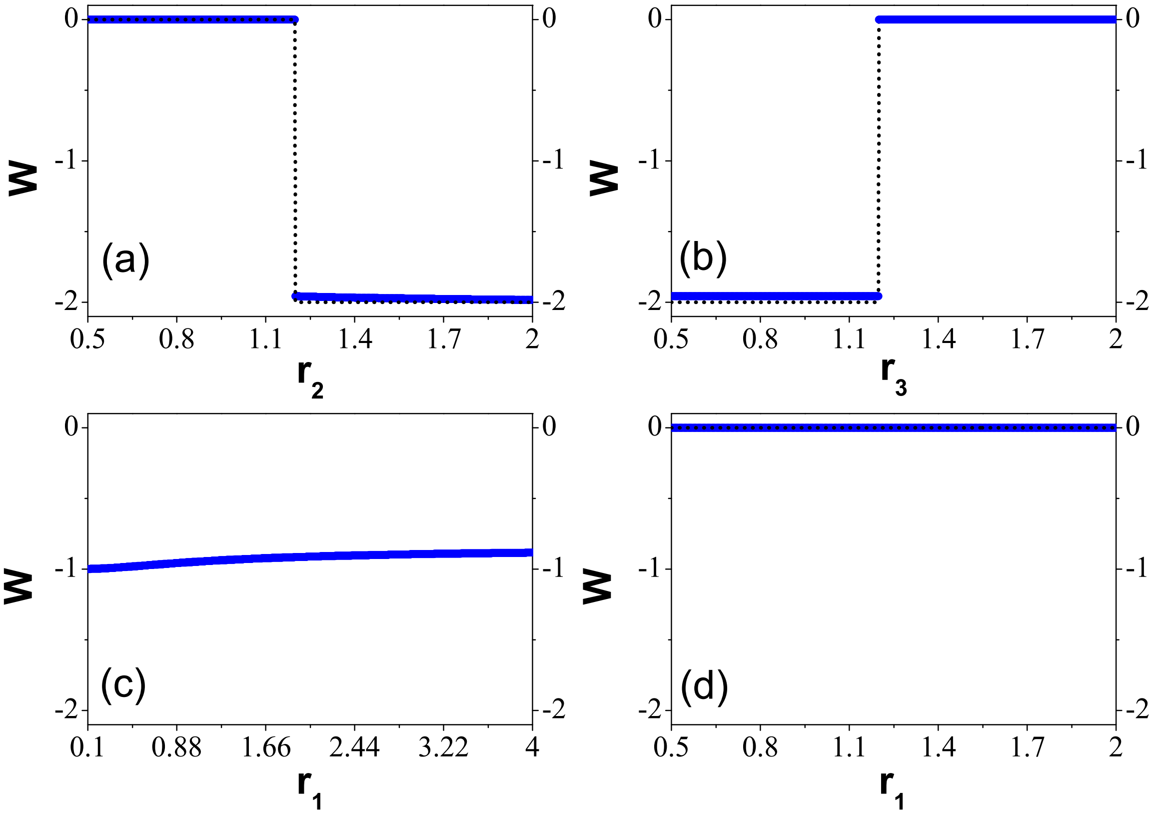

FIG. 3. The dependence of the winding number $W$ on different interaction strengths in theoretical (black) and numerical (blue). (a) $W$ against $r_2$ at $r_1 = 0.8$ and $r_3 = 1.2$; (b) $W$ against $r_3$ at $r_1 = 0.8$ and $r_2 = 1.2$; (c) $W$ against $r_1$ at $r_2 = r_3 = 1.2$; (d) $W$ against $r_1$ at $r_2 = 0.8$ and $r_3$=1.2.

state just the same as Fig. 2(c). Figure 3(d) shows $W$ against $r_1$ at $r_2 = 0.8$ and $r_3$=1.2. Clearly, $W = 0$ implies the topological states, the right edge localization states, and no topological transition is involved with $r_1$.

### C. One variant of the ALVE model

As discussed above, the topological phases of edge localization result from the competition between $r_1$ and $r_3$ flows. Now we manipulate these two types of mass flows to check the robustness of topological phases. For this aim, we modify the chain structure to the one presented in Fig. 4(a). In the variant model, the $r_1$ flow is replaced by two sub-$r_1$ flows which alternate along the chain.

We consider the mass distribution along the chain. As shown in Figs. 4(b) and 4(c), the alternation of two sub-$r_1$ flows does not alter the existence of the left and the right edge localization states. The only difference from Fig. 2 is the shrinkage of the boundary and transition regions. The edge localization states can be analyzed by the same theoretical method as that in the last subsection. Considering the alteration of the two sub-$r_1$ flows, the block Hamiltonian $\widetilde{H}(k)$ is modified to be

$$\widetilde{H}(k) = \begin{pmatrix} r_1(e^{-2ik} - e^{2ik}) & r_3 - r_2e^{-ik} \\ -r_3 + r_2e^{ik} & 0 \end{pmatrix}. \tag{10}$$

Following Eq. (6), we have the two energy bands with energy

$$E^{\pm}(k) = -ir_1 \sin 2k \pm \sqrt{-r_1^2 \sin^2 2k - r_2^2 \sin^2 k - (r_3 - r_2 \cos k)^2}, \tag{11}$$

and the corresponding left and right eigenvectors

$$|u_R^{\pm}(k)\rangle = \begin{pmatrix} E^{\pm}(k) \\ -r_3 + r_2 \cos k + ir_2 \sin k \end{pmatrix},$$
$$|u_L^{\pm}(k)\rangle = \begin{pmatrix} E^{*,\pm}(k) \\ r_3 - r_2 \cos k - ir_2 \sin k \end{pmatrix}. \tag{12}$$

Noticing the resemblance between Eqs. (10), (11), and (12) and Eqs. (4), (5), and (7), we may claim that topological phases in the variant model is independent of $r_1$ and the topological transition occurs right at $r_2/r_3 = 1$. To demonstrate it, we calculate the winding number $W$ by following the procedure from Eqs. (8) to (9). The relation between $W$ and $r_3$ (or $r_2$) is presented in Figs. 4(d) [or 4(e)]. As depicted by $W$, there still exists two distinct topological phases characterized by $W = 0$ and $W = -2$, respectively.

### IV. DISCUSSION

In this work, we studied an antisymmetric Lotka-Volterra equation defined on a chain of two-site cells with OBC.

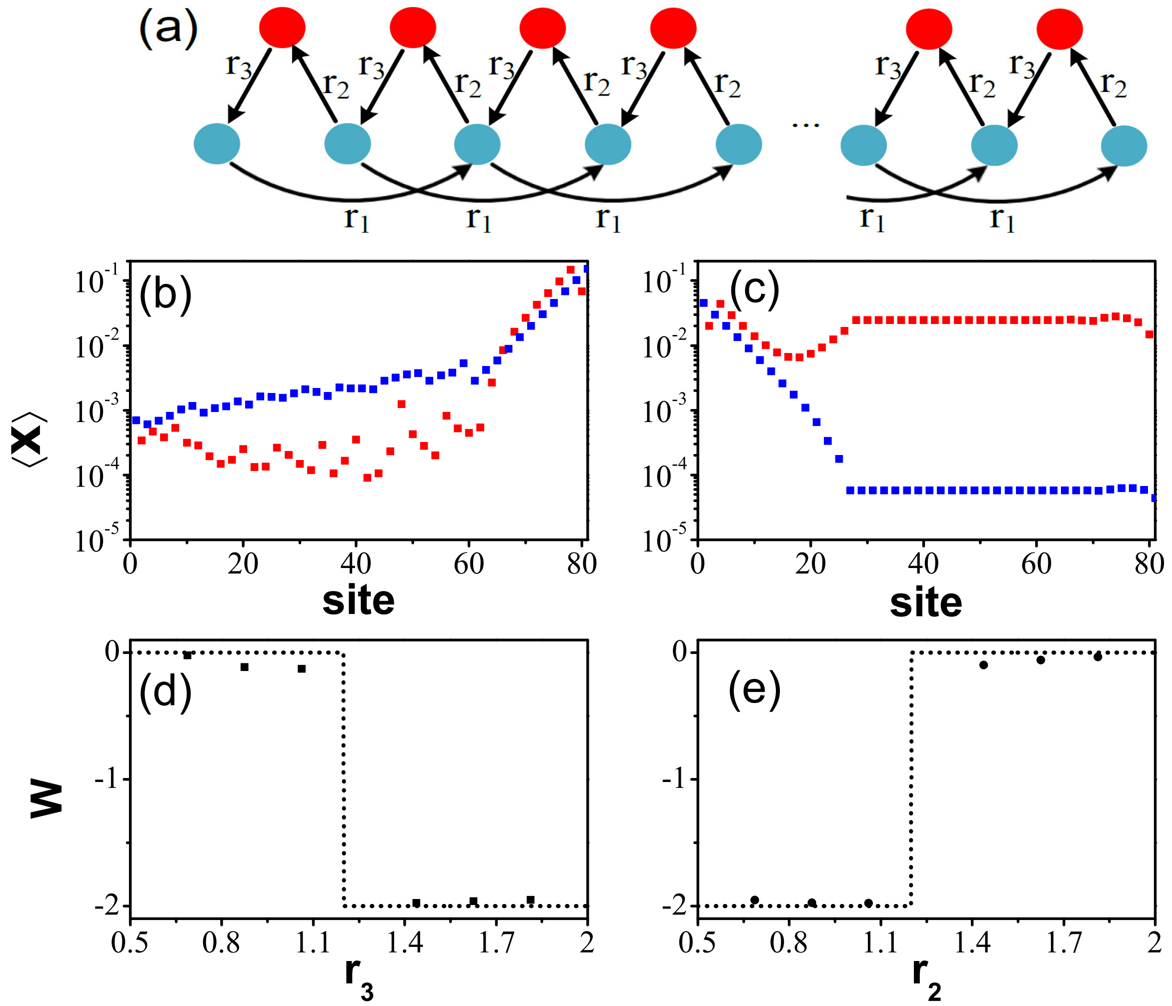

FIG. 4. (a) Schematic diagram of the chain structure of the variant model in which the $r_1$ flow is replaced by two sub-$r_1$ flows which alternate along the chain; (b) Mass distribution of the right edge localization state at $r_1 = 0.8$, $r_2 = 0.8$, and $r_3 = 1.2$; (c) Mass distribution of the left edge localization state at $r_1 = 0.8$, $r_2 = 1.2$, and $r_3 = 0.8$. The mass on the $r_1$-flow subchain is plotted in blue and the mass on the $r_3$-flow subchain in red. The winding number $W$ against $r_3$ at $r_1 = 0.8$ and $r_2 = 1.2$ is shown in (d), and $W$ against $r_2$ at $r_1 = 0.8$ and $r_3 = 1.2$ in (e). Dot lines are for theoretical results, and square and circle symbols are for numerical results in (d) and (e). The system size $S = 81$.

We found two edge-localization states which are connected by a sharp phase transition. In each edge-localization state, there exists a boundary region in which mass distribution displays an exponential decay with the distance away from the boundary. The formation of the edge-localization state is due to the competition between the two mass flows, $r_1$ and $r_3$ flows. To further comprehend the edge-localization states, we transformed the population dynamics into a non-Hermitian quantum system. Based on the generalized topological band theory of the non-Hermitian system with PBC, we found that the winding number, one type of topological invariant, can be used to distinguish the left and the right edge-localization states and to identify the transition between these two states to be a topological one. To be stressed, the transition between the left edge and the right edge localization states cannot be described as an ordinary first-order transition which requires the existence of hysteresis. The proposed reformulation from population dynamics to Non-Hermitian quantum systems here identifies the transition to be a topological one occurring right at $r_2/r_3 = 1$, which suggests that topological phases may be investigated in nonquantum systems such as population dynamics.

## ACKNOWLEDGMENTS

This work was supported by the BUPT Excellent Ph.D. Students Foundation under Grant No. CX2023106.

---

[1] H. Y. Zhou, C. Peng, Y. Yoon, C. W. Hsu, K. A. Nelson, L. Fu, J. D. Joannopoulos, M. Soljačić, and B. Zhen, Science **359**, 1009 (2018).
[2] K. Kawabata, S. Higashikawa, Z. Gong, Y. Ashida, and M. Ueda, Nat. Commun. **10**, 297 (2019).
[3] H. Y. Zhou and J. Y. Lee, Phys. Rev. B **99**, 235112 (2019).

[4] L. Li, C. H. Lee, S. Mu, and J. Gong, Nat. Commun. **11**, 5491 (2020).

[5] K. Yokomizo and S. Murakami, Phys. Rev. Lett. **123**, 066404 (2019).

[6] C. X. Liu, S. C. Zhang, and S. L. Qi, Annu. Rev. Condens. Matter Phys. **7**, 301 (2016).

[7] Z. Z. Du, H.-Z. Lu, and X. C. Xie, Phys. Rev. Lett. **121**, 266601 (2018).

[8] H. Jiang, L. J. Lang, C. Yang, S. L. Zhu, and S. Chen, Phys. Rev. B **100**, 054301 (2019).

[9] S. Longhi, Phys. Rev. B **100**, 125157 (2019).

[10] Q.-B. Zeng, Y.-B. Yang, and Y. Xu, Phys. Rev. B **101**, 241104(R) (2020).

[11] M. Z. Hasan and C. L. Kane, Rev. Mod. Phys. **82**, 3045 (2010).

[12] X. L. Qi and S. C. Zhang, Rev. Mod. Phys. **83**, 1057 (2011).

[13] C. K. Chiu, J. C. Y. Teo, A. P. Schnyder, and S. Ryu, Rev. Mod. Phys. **88**, 035005 (2016).

[14] A. Bansil, H. Lin, and T. Das, Rev. Mod. Phys. **88**, 021004 (2016).

[15] S. Yao and Z. Wang, Phys. Rev. Lett. **121**, 086803 (2018).

[16] S. Yao, F. Song, and Z. Wang, Phys. Rev. Lett. **121**, 136802 (2018).

[17] F. K. Kunst, E. Edvardsson, J. C. Budich, and E. J. Bergholtz, Phys. Rev. Lett. **121**, 026808 (2018).

[18] C. H. Lee and R. Thomale, Phys. Rev. B **99**, 201103(R) (2019).

[19] T. Helbig, T. Hofmann, S. Imhof, M. Abdelghany, T. Kiessling, L. W. Molenkamp, C. H. Lee, A. Szameit, M. Greiter, and R. Thomale, Nat. Phys. **16**, 747 (2020).

[20] L. Xiao, T. S. Deng, K. K. Wang, G. Y. Zhu, Z. Wang, W. Yi, and P. Xue, Nat. Phys. **16**, 761 (2020).

[21] T. Ozawa, H. M. Price, A. Amo, N. Goldman, M. Hafezi, L. Lu, M. C. Rechtsman, D. Schuster, J. Simon, O. Zilberberg, Rev. Mod. Phys. **91**, 015006 (2019).

[22] S. Weidemann, M. Kremer, T. Helbig, T. Hofmann, A. Stegmaier, M. Greiter, R. Thomale, and A. Szameit, Science **368**, 311 (2020).

[23] L. Huang, S. Huang, C. Shen, S. Yves, A. S. Pilipchuk, X. Ni, S. Kim, Y. K. Chiang, D. A. Powell, J. Zhu *et al.*, Nat. Rev. Phys. **6**, 11 (2024).

[24] W. D. Heiss, J. Phys. A: Math. Gen. **37**, 2455 (2004).

[25] O. Nobuyuki, K. Kohei, S. Ken, and S. Masatoshi, Phys. Rev. Lett. **124**, 086801 (2020).

[26] W. T. Xue, Y. M. Hu, F. Song, and Z. Wang, Phys. Rev. Lett. **128**, 120401 (2022).

[27] G. Chen, F. Song, and J. L. Lado, Phys. Rev. Lett. **130**, 100401 (2023).

[28] E. Tang, J. Agudo-Canalejo, and R. Golestanian, Phys. Rev. X **11**, 031015 (2021).

[29] T. Yoshida, T. Mizoguchi, and Y. Hatsugai, Phys. Rev. E **104**, 025003 (2021).

[30] J. Knebel, P. M. Geiger, and E. Frey, Phys. Rev. Lett. **125**, 258301 (2020).